

**Quantum Limited Optical Phase Detection
in a High Power Suspended Interferometer**

by

Brian Thomas Lantz

Submitted to the Department of Physics in partial
fulfillment of the requirements for the degree of

Doctor of Philosophy

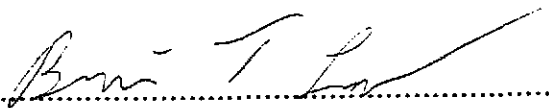
at the

MASSACHUSETTS INSTITUTE OF TECHNOLOGY

February, 1999

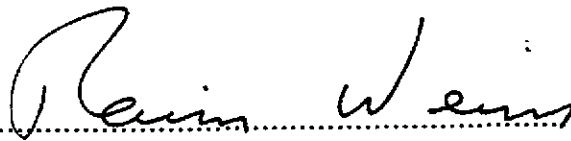
© Massachusetts Institute of Technology, 1999. All Rights Reserved.

Author



Department of Physics
February, 1999

Certified by



Rainer Weiss
Department of Physics
Thesis Supervisor

Accepted by

Thomas J. Greytak
Professor, Associate Department Head for Education
Department of Physics

Quantum Limited Optical Phase Detection in a High Power Suspended Interferometer

by

Brian Lantz

Submitted to the Department of Physics in February 1999,
in partial fulfillment of the requirements for the degree of
Doctor of Philosophy

Abstract

The LIGO project (Laser Interferometer Gravitational-Wave Observatory) is currently engaged in the construction of a new observatory to measure gravitational radiation from astrophysical sources. The first generation of interferometric gravitational wave antennas is scheduled to come on-line in 2001. With an initial noise level of 3×10^{-23} strain/ $\sqrt{\text{Hz}}$ at frequencies around 200Hz, these antennas represent the most sensitive instruments ever constructed for the detection of gravitational radiation. To achieve the required sensitivity, the antennas are configured as recycled Michelson Interferometers with Fabry-Perot cavities in the Michelson arms.

One of the fundamental limits associated with an instrument of this type is the ability to detect differential phase shifts between the beams returning to the beamsplitter from the Fabry-Perot arm cavities. To achieve the planned sensitivity to gravitational radiation, this detection should be limited only by photon counting statistics ("shot noise") at a level of 8×10^{-11} radians/ $\sqrt{\text{Hz}}$ between 150Hz and 10kHz.

The goal of this work is to develop and demonstrate the techniques which are necessary to achieve this optical phase sensitivity. A prototype recycled Michelson interferometer was constructed which reached an optical phase sensitivity of 12×10^{-11} radians/ $\sqrt{\text{Hz}}$ above 600 Hz.

This thesis describes the methods used to achieve this optical phase sensitivity, and details the lessons learned from operating the prototype instrument. We pay particular attention to interferometric control of suspended optics, laser frequency control, and thermal lensing.

Thesis Supervisor: Rainer Weiss
Title: Professor of Physics

Acknowledgments

To Rai, who talked with me one Saturday morning and set me off in a new direction.

To Peter Fritschel, whose quiet brilliance made this experiment possible.

To Gaby, who must be the best lab partner one could hope for.

To Partha and Haisheng, who worked tirelessly to make this project a success.

To Nergis and Daniel, for a damn fine wavefront sensor which worked on the first day!

To Jim, Rich, and Rick, who gave us the Prestabilized Laser. Either it ran like a champ, or Rich would fly to Boston and fix it.

To the LIGO team, for the technical support, guidance, and friendship which made this experiment a success. You will change the world, good luck!

To Jen, the love of my life and the light of my heart, my constant companion, even when I was writing my thesis.

“In the first experiment one of the principal difficulties encountered . . . was its extreme sensitiveness to vibration. This was so great that it was impossible to see the interference fringes except at brief intervals when working in the city, even at two o’clock in the morning.”

-Albert Michelson, [Michelson 1887]

(Describing the first interferometer he used to attempt to detect the luminiferous ether.)

Table of Contents

	<u>page</u>
List of Figures	11
Chapter 1: Importance of Optical Phase Sensitivity to Interferometric Gravitational Wave Antennas	13
1.1: Introduction	13
1.2: Gravitational Waves	13
1.3: Sources of Gravitational Waves	15
1.4: The LIGO detector	17
Chapter 2: Interferometer Configuration and Sensitivity Limits	21
2.1: Michelson Interferometer Sensitivity and Schnupp Modulation	21
2.2: Power Recycling Cavity	26
2.3: Useful Expressions	30
2.4: Noise	31
2.5: Sensitivity limit for modulation readout scheme with optical losses	35
Chapter 3: Description of the Experiment	39
3.1: Configuration of the Interferometer	39
3.2: The Differential Mode and the Detection of Optical Phase	40
3.3: The Common Mode and the Importance of Frequency Noise	43
3.3.1: Coupling of Frequency Noise into Phase Noise	43
3.3.2: The Prestabilized Laser	43
3.3.3: Cavity Common Mode Control, the Second Stage of Frequency Control ..	46
3.4: Wavefront Sensing and Control of the Suspended Interferometer	52
3.5: Environmental Isolation of the Interferometer Optics	55
3.5.1: Interferometer Optics	56
3.5.2: Parasitic Interferometry	61
Chapter 4: Thermal Lensing of the Beamsplitter	69
4.1: Measuring the Thermal Distortions	69
4.2: Modeling of the Thermal Lens	72
4.2.1: Thermal Lens parameters	72
4.2.2: Propagation Model	75
Chapter 5: Phase Sensitivity and Phase Noise	83
5.1: Measurement of the Optical Phase Sensitivity	83
5.2: Result of the Measurement	83
5.2.1: Shot Noise Limited Regime	84
5.3: Spectral Features	87
5.3.1: Thermal Motion of Magnetic Actuator Fins	88
5.3.2: Calibration peak at 2kHz	89
5.3.3: Motion of Optics on Input Table	89
5.3.4: Violin Modes of Suspension Wires	90
5.3.5: Power Line Noise	90
5.4: Low Frequency Noise	90
5.4.1: Electronic Noise	90
5.4.2: Thermal Noise	93

5.4.3: Beam Jitter	97
5.4.4: Input Power Fluctuations	105
Chapter 6: Conclusions	109
6.1: Improvements in Optical Phase Measurements	109
6.2: Improvements from the Spectrum of the Argon Laser Experiment	111
6.3: Limiting Noise for this Experiment	111
6.4: Concluding Remarks	115
References	117

List of Figures

	<u>page</u>
Figure 1.1: The effect of a passing gravitational wave on an object.	15
Figure 1.2: Basic optical configuration of LIGO.	18
Figure 1.3: LIGO noise curve.	20
Figure 2.1: Schematic view of recycled Michelson interferometer with frontal modulation.	21
Figure 2.2: Schematic view of an asymmetric Michelson interferometer.	22
Figure 2.3: Fields within a Fabry-Perot cavity	26
Figure 2.4: Field Eigenstates described by equations 2.40 through 2.42.	32
Figure 2.5: Plot of $(N_2 \pm \Delta N_2) / N$ vs. differential phase for $N=400$	34
Figure 3.1: Optical Configuration of the Phase Noise Interferometer.	39
Figure 3.2: Overview of the experimental layout.	41
Figure 3.3: Open loop gain of differential Michelson interferometer control loop.	42
Figure 3.4: Schematic drawing of the Prestabilized Laser.	44
Figure 3.5: Open loop gain of the Prestabilized Laser	45
Figure 3.6: Frequency noise of the Prestabilized Laser	46
Figure 3.7: Common mode servo control.	47
Figure 3.8: Servo paths for common mode servo.	49
Figure 3.9: Open loop gain of the second stage of frequency control.	50
Figure 3.10: Suppression of frequency noise by the common mode loop.	51
Figure 3.11: Frequency noise of laser light in the power recycling cavity.	52
Figure 3.12: Alignment of quadrant diode for wavefront sensor measurement.	53
Figure 3.13: Open loop gain of the differential angular alignment servo.	54
Figure 3.14: Detail of unity gain point for alignment control servo.	55
Figure 3.15: Environmental isolation of the experiment.	56
Figure 3.16: Closed loop gain for one foot of the Stacis™ system supporting the Michelson optics.	57
Figure 3.17: Seismic isolation stack.	58
Figure 3.18: Optic suspended by a single loop of wire.	59
Figure 3.19: OSEM detail.	60
Figure 3.20: Suspension wire attachment detail.	61
Figure 3.21: Electric fields of a parasitic interferometer.	61
Figure 3.22: Seismic isolation of the input optics table.	63
Figure 3.23: Horizontal motion of input optics table	64
Figure 3.24: Acoustic drive level at the output optics table, with and without anechoic enclosure.	66
Figure 4.1: Measured contrast loss of the beamsplitter as a function of incident power.	71
Figure 4.2: Schematic view of the heat flow from surface absorption of the beamsplitter.	73

Figure 4.3: Thermal distortion of the beamsplitter for power absorbed at one surface.	73
Figure 4.4: Thermal distortion of the beamsplitter caused by bulk absorption.	74
Figure 4.5: Diagram listing the steps of the beam propagation model.	75
Figure 4.6: Measured contrast loss and predicted contrast loss with 47 ppm/cm bulk absorption.	76
Figure 4.7: Modeled intensity distribution of the dark fringe.	77
Figure 4.8: Image of dark port beam with 5 watts of circulating power in the interferometer.	79
Figure 4.9: Dark port image with 21 watts of circulating power.	79
Figure 4.10: Dark port Image with 36 watts of circulating power.	80
Figure 4.11: Dark port Image with 57 watts of circulating power.	80
Figure 4.12: Dark port image with 98 watts of circulating power.	81
Figure 5.1: Schematic view of Michelson interferometer readout and control configuration.	83
Figure 5.2: Spectrum of the Phase Noise Interferometer.	84
Figure 5.3: Cavity Loss (L) and Cavity Matching parameter (M) calculation.	86
Figure 5.4: Narrow spectral features.	88
Figure 5.5: Drawing of an interferometer optic, showing the magnet-fin assemblies.	89
Figure 5.6: Impact of coil driver noise on the spectrum.	91
Figure 5.7: Impact of Michelson controller noise on the spectrum.	92
Figure 5.8: Total electronic noise.	92
Figure 5.9: Detail of spectrum showing the 3 peaks associated with fin resonances.	95
Figure 5.10: Impact of Thermal Motion on Spectrum.	96
Figure 5.11: Detail of figure 5.10, showing impact of thermal motion of violin modes.	97
Figure 5.12: Optical lengths and misalignments in the Michelson interferometer.	98
Figure 5.13: Residual differential misalignment of the Michelson arm mirrors.	100
Figure 5.14: Angular motion of input beam measured on the input optics table.	101
Figure 5.15: Geometry of the recycling cavity.	101
Figure 5.16: Impact of misalignments on phase noise spectrum.	103
Figure 5.17: Relative fluctuations of the power in the recycling cavity.	107
Figure 5.18: Impact of power fluctuations on phase noise spectrum.	107
Figure 6.1: Evolution of optical phase measurements.	109
Figure 6.2: Comparison of the phase noise spectra with the LIGO requirement.	110
Figure 6.3: Major noise sources in the measurement.	112
Figure 6.4: Major noise sources at low frequencies.	113
Figure 6.5: The residual phase noise in this measurement.	114

Chapter 1

Importance of Optical Phase Sensitivity to Interferometric Gravitational Wave Antennas

1.1 Introduction

The Laser Interferometer Gravitational-Wave Observatory (LIGO) is now engaged in construction of a new observatory which will be able to measure gravitational radiation from astrophysical sources [Abramovici '92]. Gravitational radiation was first predicted by Einstein [Einstein '16], [Einstein '18], but, due to the extremely small influence of this radiation, it has never been directly observed.¹ The goal of this chapter is to introduce the reader to effects of gravitational radiation, explain briefly the method which LIGO will use to detect this radiation, and motivate this work by describing the importance of optical phase sensitivity to the LIGO detection scheme.

1.2 Gravitational Waves

Gravitational waves are traveling waves of the space-time metric, $g_{\mu\nu}$. Generated by accelerating masses, these gravitational field disturbances propagate at the speed of light, and provide the solution to Newton's problem of gravitational action at a distance. A gravitational plane wave creates a differential strain along the 2 space axes which are transverse to the direction of the waves's propagation. For any reasonable source of gravitational radiation, the perturbations of the metric by the passing gravitational wave are quite small, so we use the "linearized" theory (see, for example, [Schutz '90] or [Saulson '94]) and rewrite the metric $g_{\mu\nu}$ as

$$g_{\mu\nu} \approx \eta_{\mu\nu} + h_{\mu\nu} \quad |h_{\mu\nu}| \ll 1 \quad (1.1)$$

where $\eta_{\mu\nu}$ is the Minkowski metric (describing flat space), and $h_{\mu\nu}$ is the metric distortion due to the gravitational wave. In the weak-field limit, the Einstein equation for $h_{\mu\nu}$ can be written as a traveling wave equation,

1. However, indirect observations have been made by Hulse & Taylor [Hulse '75], [Taylor '82], [Taylor '89], who carefully studied the orbital decay of a neutron star binary system, and found the decay rate to be in excellent agreement with the energy lost to gravitational radiation.

$$\left(-\frac{1}{c^2} \frac{\partial^2}{\partial t^2} + \nabla^2 \right) h_{\mu\nu} = 0. \quad (1.2)$$

In a transverse-traceless gauge, we can write the solution for a wave traveling in the \hat{z} direction as

$$h_{\mu\nu} = \exp(ik_\alpha x^\alpha) \begin{bmatrix} 0 & 0 & 0 & 0 \\ 0 & h_+ & h_x & 0 \\ 0 & h_x & -h_+ & 0 \\ 0 & 0 & 0 & 0 \end{bmatrix}. \quad (1.3)$$

This represents two independent plane-wave solutions. The magnitude of the spatial components along h_{xx} and h_{yy} is h_+ , which is known as the “plus” polarization, and the magnitude along h_{xy} and h_{yx} is h_x , which is commonly called the “cross” polarization. Eqn. 1.3 means that each of the four non-zero components of $h_{\mu\nu}$ could be expressed as

$$h_{xx} = h_+ \cdot \sin(-\omega t + kz) \quad (1.4)$$

representing a metric perturbation traveling along \hat{z} at the speed of light, with frequency ω , and amplitude h_+ .

One way to understand the implication of a passing gravitational wave is to examine the change in proper distance between two objects as a wave passes by. With one object at the origin, and the second at $x = l$, $y = z = 0$, then the proper distance between them is

$$D_{\text{proper}} = \int \left| g_{\mu\nu} dx^\mu dx^\nu \right|^{\frac{1}{2}}. \quad (1.5)$$

This reduces to

$$D_{\text{proper}} = \int_0^l \sqrt{|g_{xx}|} dx \quad (1.6)$$

If h_+ is spatially uniform, changing slowly², and less than 1, then the proper distance is:

$$\begin{aligned} D_{\text{proper}} &\approx l \cdot \sqrt{\eta_{xx} + h_{xx}(x=0, t=0)} \\ &\approx l \cdot \left[1 + \frac{1}{2} h_+(x=0, t=0) \right] \end{aligned} \quad (1.7)$$

2. The measurement in LIGO will be conducted by light which is resonant in a 4km arm cavity, so the time fluctuations of $h_{\mu\nu}$ should be compared with the cavity storage time of 0.88 msec.

which means the distance between the two “freely-falling” objects changes as a gravitational wave passes by. According to eqn. 1.3, $h_{xx} = -h_{yy}$, so as distances along the \hat{x} axis are elongated, distances along \hat{y} will be compressed by the same ratio. It is important to realize that the proper distance is stretched by an amount which is proportional to the original distance and the gravitational wave amplitude, which is why the effect of gravitational radiation is usually described as producing a strain, i.e.

$$\frac{\delta l}{l} = \frac{1}{2}h_+ \quad (1.8)$$

There are only two independent components of $h_{\mu\nu}$, which are described as the two polarizations of gravitational waves. The amplitude of a plane wave in the “plus” polarization is captured by h_+ , which will differentially change the proper distances along \hat{x} and \hat{y} . The “cross” polarization is described by h_x , and results in a differential stretching which is rotated by 45° from the \hat{x} and \hat{y} axes. This effect on a ring of free masses is shown in figure 1.1.

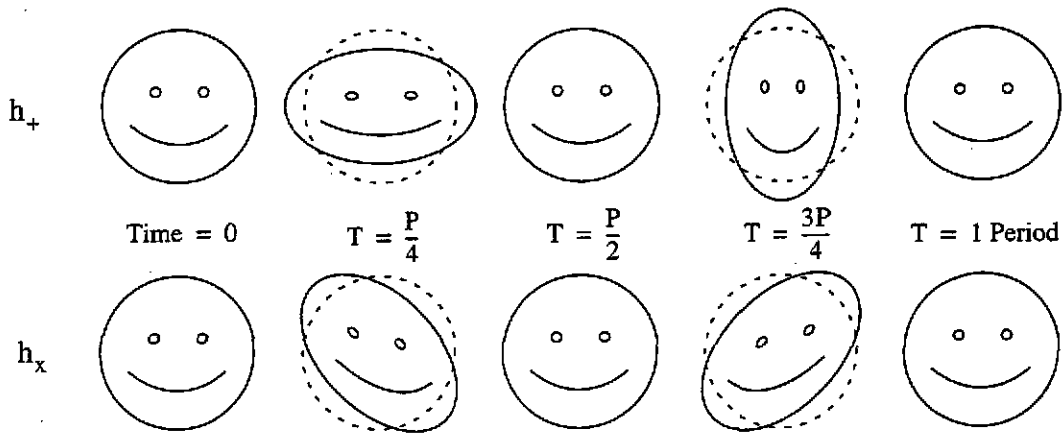


Figure 1.1: The effect of a passing gravitational wave on an object.

1.3 Sources of Gravitational Waves

The search for gravitational waves has so far been stymied by the fact that even the most powerful sources of gravitational radiation only produce tiny effects at the Earth. A typical source produces waves at the earth with a strain of $h \sim \frac{\ddot{Q}G}{Rc^4}$. Here, \ddot{Q} is the acceleration of the quadrupole moment of the source, G is the gravitational constant, R is the distance from the source, and c is the speed of light. The scaling factor, G/c^4 , is quite small, leading us to consider gravitational radiators on the order of a solar mass.

Many sources of gravitational waves are discussed as possible LIGO candidates, including coalescence of two compact objects (such as neutron stars or black holes), supernovas which generate non-spherical motion during the core collapse, and spinning neutron stars with non-axisymmetric mass distribution (see, for example, [Thorne '87]). The imminent completion of the LIGO interferometers and data from the new Rossi X-Ray Timing Explorer (RXTE) have generated a great deal of interest in variants to these standard sources, including new estimates of the number of neutron star-black hole binaries by Bethe and Brown [Bethe '98] and work by Lars Bildsten and others discussing various mechanisms by which neutron stars could convert the energy and angular momentum gained by accretion into gravitational radiation [Andersson '98], [Bildsten '98], [Owen '98].

The fiducial source of radiation for which one designs detectors is the burst of gravitational waves produced in the final minutes before the coalescence of inspiralling binary neutron stars. If two neutron stars of equal mass M are orbiting in the x - y plane at a distance $2r_0$ from each other with an orbital frequency of f_{orb} , then the amplitude of waves traveling along the \hat{z} axis is [Saulson '94]

$$h_{xx} = \frac{32\pi^2 G}{Rc^4} M r_0^2 f_{\text{orb}}^2 \cos(2 \cdot 2\pi f_{\text{orb}} t), \quad (1.9)$$

$$h_{xy} = -h_{xx}.$$

Newtonian mechanics suggests we can relate the radius and frequency by $f_{\text{orb}}^2 = GM/16\pi^2 r_0^3$, and the strain becomes

$$h_{xx} = \frac{2G^2 M^2}{Rc^4 r_0} = 1.1 \times 10^{-21} \left(\frac{M}{1.4M_\odot} \right)^2 \left(\frac{15 \text{ Mpc}}{R} \right) \left(\frac{f_{\text{orb}}}{400 \text{ Hz}} \right)^{\frac{2}{3}}. \quad (1.10)$$

This represents the strain produced by a pair of neutron stars ($M = 1.4M_\odot$) in the Virgo cluster ($R = 15 \text{ Mpc}$) in the last minute of their lives (when $f_{\text{orb}} \sim 400 \text{ Hz}$!). It is this level of strain which LIGO hopes to detect. Unfortunately, current estimates of the population of neutron star binaries indicate that we will need to observe an astrophysical volume which extends 200 Mpc from Earth to measure three such coalescence events each year ([Phinney '91] and [Narayan '91]).

Another burst source is the core collapse of a type II supernova. Several models of core collapse are described in [Thorne '87]. The current belief is that the core collapse will be only slightly aspheric. If bar ($m=2$) modes form in the spinning, collapsing core, they would emit gravitational radiation. These events might last about 30 cycles at 1000Hz, and could emit gravitational energy $\Delta E_{\text{GW}} \sim 3 \times 10^{-4} M_{\odot} c^2$. At a distance of 10Mpc, within which volume there are typically several type II supernovas each year, a core collapse which develops a bar instability could generate a characteristic strain at the Earth of $h_c \sim 5 \times 10^{-22}$.

There are several models for periodic sources, sources whose gravitational radiation signature changes very slowly with time. Many of these sources, like the Hulse-Taylor binary pair of neutron stars PSR1916+13, emit radiation at a frequency much to low to be seen with currently imagined Earth-bound instruments³. Some periodic sources have been suggested, however, which would be within the observational capabilities of the LIGO detectors. [Bildsten '98] has suggested, for example, that the accreting neutron star in Scorpius X-1 could be emitting gravitational waves at 500Hz, twice the neutron star rotation frequency. The amplitude could be as large as $h_c \approx 2.2 \times 10^{-26}$, which means it should be observable with a year or so of integrated observation time.

1.4 The LIGO detector

To detect a strain of the order 10^{-21} will be difficult, but several groups around the world are currently building observatories to meet that challenge. LIGO is building a pair of 4km baseline optical interferometers, one in Hanford, Washington, and one in Livingston Parish, Louisiana [Barish '97]. LIGO is also building a half length (2 km) interferometer in the vacuum system at the Hanford site. Virgo, an Italian-French collaboration, is building a 3km instrument near Pisa, Italy [Vinet '97]. GEO600 is a German-U.K. collaboration building an advanced 600 meter instrument in Hanover, Germany [Danzmann '97]. There is also active work ongoing at the TAMA project in Japan [Tsubono '97] and the ACIGA project in Australia [Blair '97].

Each of the LIGO instruments is configured as a power-recycled Michelson interferometer with Fabry-Perot arm cavities, as shown in figure 1.2. The Michelson interferome-

3. However, LISA, the proposed Laser Interferometer Space Antenna, could readily observe many low frequency sources within our galaxy [Folkner '98].